Development of a Superconducting Memory Device based on Magnetic Spin Texture

Scheinowitz, Naor

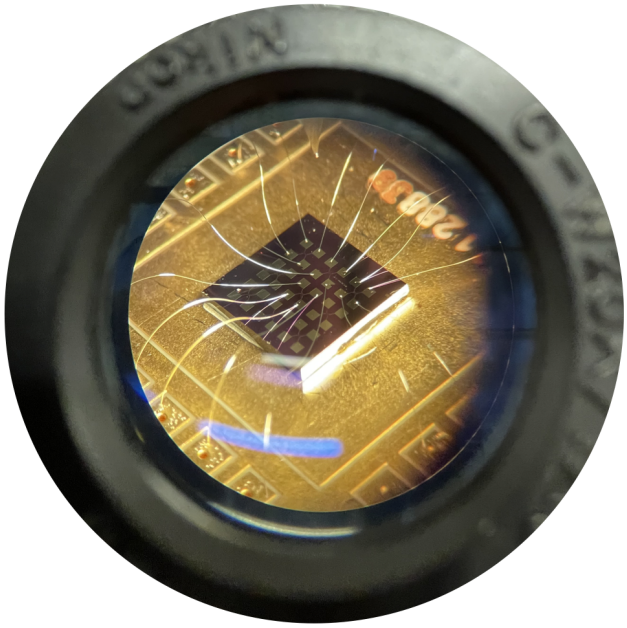

Development of a Superconducting Memory Device based on Magnetic Spin Texture

THESIS

submitted in partial fulfillment of the
requirements for the degree of

MASTER OF SCIENCE
in
PHYSICS

Author :	N.M.A. Scheinowitz
Student ID :	1531921
Supervisor :	Prof.dr. J. Aarts
	Dr. K. Lahabi
	R. Fermin MSc.
2^{nd} corrector :	Dr. W. Löffler

Leiden, The Netherlands, August 6, 2021

Development of a Superconducting Memory Device based on Magnetic Spin Texture

N.M.A. Scheinowitz

Huygens-Kamerlingh Onnes Laboratorium, Universiteit Leiden
P.O. Box 9500, 2300 RA Leiden, The Netherlands

August 6, 2021

Abstract

In order to curb the growing energy demand and environmental impact of data centers, breakthrough technologies bringing increased energy efficiency are required. Superconducting computing promises massive energy savings through near-dissipationless operation. So far, multiple designs for superconducting memory are proposed, but none meets all requirements for an implementable device. To this end, we propose a novel design of superconducting memory (SCM) device, using two stable magnetic spin textures in a single-layer elliptical SFS Josephson junction. We observe a change in critical current between the two states by a factor of five at remanence. Using a novel technique to quantify the effects of stray fields using micromagnetic simulations, we conclude that the shift in critical current is caused by a large contrast in stray field strength between the two magnetic states. Furthermore, we verify that the switching process is deterministic and unambiguous during read-out. Future pathways to scale up this memory device are proposed.

Cover picture: Picture taken through an optical microscope showing a silicon wafer with nine sample devices, electronically connected a sample holder.

Contents

Chapter 1

Introduction

Continued emissions of greenhouse gasses and subsequent anthropogenic climate change is nearing critical tipping points that will further accelerate the heating of our planet. As the effects of these tipping points are likely to be irreversible, global effort should be put on reducing emissions by transitioning to renewable and emission-free energy sources, while simultaneously reducing energy use by prioritization and increased efficiency. [1]

Digitisation is often presumed to increase efficiency across sectors. However, recent research has found the opposite to be true. [2] Making matters worse, total energy consumption by the ICT sector is projected to grow to between 8% and 21% of an increasing global energy demand between 2015 and 2030, despite expected gains in hardware efficiency. Power hungry data centers, already consuming 200 TWh each year, are one of the main contributors to this growth. [3, 4] As demand for cloud services is not likely to decrease and the transition to renewables has so far not been able to keep up with increases in energy demand, breakthrough computational technologies are required. [5]

One candidate technology for data center applications is superconducting computing. Conventional computers consume energy in large part due to Ohmic resistance, with subsequent heat dissipation requiring active cooling, adding to the energy demand. Replacing these machines with superconducting equivalents would eliminate this process entirely, leading to enormous energy savings, even accounting for cryogenic cooling.

Current designs for superconducting hardware operate through various implementations of Josephson junctions. Recent development in superconducting logic has reached the point of implementable prototypes [6], but superconducting memory has so far not reached the same level. Most proposals for superconducting memory devices work by manipulating the (critical) current that passes through a Josephson junction, but the manipulation mechanism differs between designs. The most common factor is that Josephson junctions with multiple ferromagnetic layers are used as pseudo-spin-valve devices, where the change in critical current defines the two states for a memory device. While most designs show promising performance in one metric, none manage to satisfy all requirements for an implementable device confidently. Some are highly scalable but volatile [7, 8], others are non-volatile but either produce low changes in critical current [9–11], or require a complex construction [12–14]. Others still may be easily disturbed by low external magnetic fields [15].

In this thesis, we present a novel technique for storing information in a SFS Josephson junc-

tion. Instead of storing bits by the mutual orientation of multiple ferromagnetic layers, we use different spin textures in a single layer. We achieve this results by designing the geometry of the junction using micromagnetic simulations, such that the ferromagnetic layer contains two distinct stable magnetic states at remanence. The resulting device allows between the states by applying external magnetic fields on the order of 40 mT. The stray fields originating from the different spin textures penetrate the junction area to modulate the amount of critical current it can sustain, thus creating two electrically identifiable states.

We show that our device succeeds in multiple metrics for superconducting memory: the memory is highly non-volatile as the information is stored magnetically and not through a superconducting process, it is resistant to disturbances by low magnetic fields but does not require large switching fields, and the change in critical current is on the order of a factor 5, making the two states easily identifiable. In this thesis, we discuss the design process of the device and show how we verified that it functions as a superconducting memory.

Chapter 2

Background

The potential benefits of superconducting computing are plentiful. From an economic perspective, the prospect of increased energy efficiency and associated cost savings can make existing businesses more profitable. Similarly, environmentalists will welcome the energy savings as a means to a more sustainable future. Additionally, superconducting computing may play an important role in the development of quantum computing, a subject many a scientist cherish.

With much to gain from an implementable superconducting memory device, it is not surprising that in recent years many research groups have proposed designs for it. However, for a memory device to be implementable, it must perform well in four metrics.

1. The device must contain two states that are clearly separated and thus easily identifiable.
2. The switching mechanism between the two states must be reliable, predictable, and practical. In other words: switching between the states should be deterministic and require low amounts of energy.
3. The memory must be non-volatile.
4. The device should be scalable.

In this chapter, we give a general overview of the different current proposals for superconducting memory (SCM) devices and show how they perform in the aforementioned metrics. We will also briefly introduce the theoretical concepts required to interpret the results in chapter 4. We will focus on key results from the BCS and Ginsburg-Landau theories on superconductivity and the basic principles of Josephson junctions. For an in-depth explanation of these covered topics, readers are encouraged to study the work by Tinkham (2004). [16]

2.1 Current Proposals for Superconducting Memory

The many different designs for SCM devices can be divided into two main categories. The first type makes use of some superconducting process to create two different states. Figure 2.1 shows an example of a design containing a vortex trap. The presence or absence of a superconducting vortex changes the amount of current that can be passed through the device, defining the two memory states. Another example is shown in figure 2.2, where a persistent current in a superconducting loop is used. Here the sign and/or magnitude of the persistent current defines the different states.

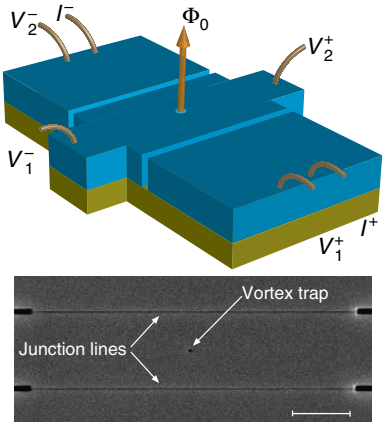

Figure 2.1: *Example of a memory device where the presence or absence of a superconducting vortex defines two states. Image taken from Golod et al. (2015) [8].*

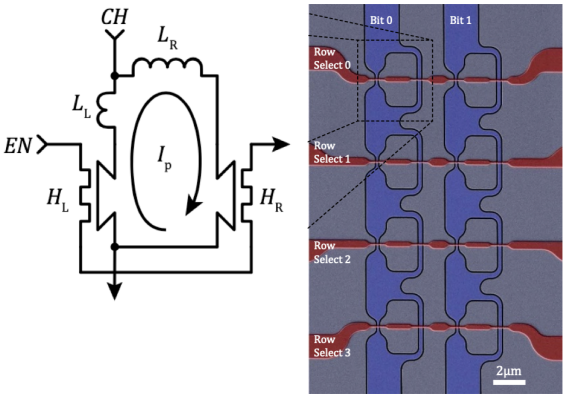

Figure 2.2: *Example of a memory device where the sign and/or magnitude of a persistent current in a loop defines two states. The bottom image shows the device in an array configuration. Image taken from Butters et al. (2021) [7].*

Despite showing some great potential for scalability (see bottom of figure 2.2), these devices have a fundamental drawback: information is stored purely through superconductivity. If the device heats up above its critical temperature, even momentarily, all information is lost, making these devices inherently volatile. [7, 8]

The second type of SCM consists of multilayer Josephson junctions. In these devices, the weak link in a Josephson junction is made up of multiple ferromagnetic layers, see figure 2.3. The mutual magnetic orientation of these layers modulates the amount of current that can pass through the junction. One can then define two states based on the parallel or anti-parallel magnetic orientation. Switching between these orientations is achieved by applying external magnetic fields.

Unlike the first type of SCM devices, multilayer junctions do not suffer from temperature volatility. Information stored magnetically should be stable up to the Curie temperature of the ferromagnetic materials, which in most cases exceeds superconducting temperatures by multiple orders of magnitude. However, multilayer SCM devices do have their own drawbacks. Stray fields cause interlayer coupling between the ferromagnetic layers, making it difficult to change the magnetic orientation of one layer without changing the other. This often results in either unreliable switching, large switching fields, or both. Additionally, these type of devices often do not produce large changes in critical current. Figure 2.4 shows such an example; at zero applied fied, the difference in critical current between the two states is small. [9–15]

2.2 Superconductivity: Key Concepts

A foundational principle of quantum mechanics is that states are not described in absolute terms but by probabilities enclosed in wavefunctions. To understand the properties of a conducting system, one needs a wavefunction describing the behavior of the particles producing a current. In the case of conventional conductors, this role is fulfilled by electrons. These 1/2-spin particles are relatively easy to describe in isolation, but the complexity grows rapidly in multi-electron systems because fermions cannot occupy identical quantum states. In bulk materials, the number of particles is in the order of the Avogadro constant $N_A \approx 6 \times 10^{23}$, making

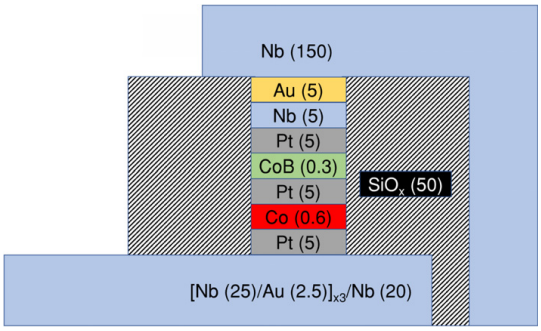

Figure 2.3: *Example construction of a multilayer Josephson junction. Image taken from Satchell et al. (2020) [9].*

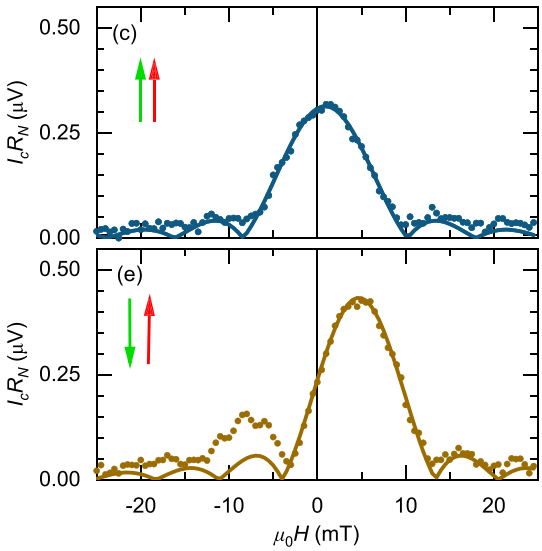

Figure 2.4: *Diffraction patterns for two different magnetization orientations in the multilayer junction of figure 2.3. Image taken from Satchell et al. (2020) [9].*

it futile to attempt to calculate a complete macroscopic wavefunction.

In the 1950's, two important theories on superconductivity emerged: the phenomenological Ginzburg-Landau theory and the microscopic BCS theory, named after Bardeen, Cooper and Schrieffer. BCS theory describes how electrons near the Fermi surface form *Cooper Pairs* through the presence of an attractive potential. In most superconductors, this attraction is the result of electron-phonon interaction. Unlike single electrons, Cooper pairs feature an integer spin, allowing them to occupy a shared ground state, forming a so-called Bose-Einstein condensate. This condensate can be described by a *single macroscopic wavefunction*. This wavefunction can be written in the general form

$$\Psi(r,t) = \sqrt{n_s(r,t)}\, e^{i\varphi(r,t)}\,, \tag{2.1}$$

such that $|\Psi|^2 = n_s$ is the probability density of the spatial distribution of Cooper Pairs.

The Ginsburg-Landau theory allows us to characterize superconductors by two distinct lengthscales: the coherence length ξ and the penetration depth λ. The former describes the distance over which the superconducting wavefunction can spatially vary with minimal change in energy, the latter gives a measure for how deep an external magnetic field can penetrate the superconducting surface.

These length scales mark features unique to superconductors. External magnetic fields are expelled (up to a critical field B_c) by persistent currents in a λ thick layer from the surface in what is known as the *Meissner effect*. Additionally, the wavefunction cannot discontinuously vanish at an interface with a non-superconducting metal, as its change is limited by the coherence length. This causes it to 'leak' into the adjacent material, see figure 2.5. This *proximity effect* can turn normal metals superconducting over the length scale of their respective coherence length ξ_n, dependent on temperature and the relevant metal diffusion constant. This effect will prove fundamental for the design of our memory device in chapter 4.

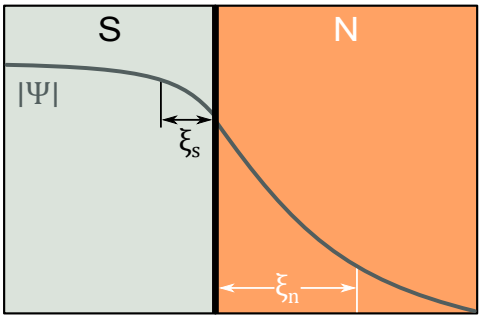

Figure 2.5: *Schematic demonstrating the proximity effect between a superconductor and a normal metal [17].*

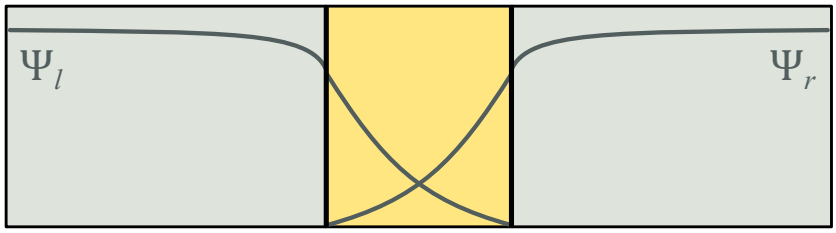

Figure 2.6: *Schematic of a Josephson junction with two superconducting electrodes (green) separated by a weak link (yellow) [17].*

2.3 Josephson junctions

Two superconductors can be connected with one another through a non-superconducting region due to the proximity effect. This can be seen in figure 2.6 as two macroscopic wavefunctions that overlap in a proximized weak link. The weak link separating the electrodes can be constructed by any number of materials: insulators (SIS junction), normal metals (SNS), ferromagnets (SFS) or even normal state superconductors (SsS) (e.g. constrictions and ultra-thin superconductors). Since the amplitude of the wavefunction is directly related to the number density of Cooper pairs (equation 2.1), this means Cooper pairs are in fact transferred between the two superconductors. Such a system is called a Josephson junction.

The amount of supercurrent that can pass through a Josephson junction depends on the phase difference of the wavefunctions on either side of the weak link. This is summarized in the current-phase relation known as the *Josephson Effect*:

$$I(\Delta\varphi) = I_c \sin(\Delta\varphi)\,, \tag{2.2}$$

where I_c is the critical current, the maximum supercurrent that can pass through the junction. This value can be measured experimentally by applying a bias d.c. current through a junction while measuring the voltage. The critical current is then identified in this I-V as the maximum current where the voltage is zero (no resistance).

Josephson junctions have a property that allows researchers to identify them unambiguously. When exposed to radio frequency (RF) radiation, an additional RF supercurrent is induced in the junction. These can be observed as 'steps' in the I-V characteristic of the junction at integer multiples of $V = f\Phi_0$, where f is the radiation frequency and Φ_0 is the magnetic flux quantum. Figure 2.7 shows an example of these so-called *Shapiro Steps*.

The wavelike nature of a Josephson junction introduces another wavelike phenomenon, analogous to optics. A single slit irradiated with coherent light will produce a Frauenhofer diffrac-

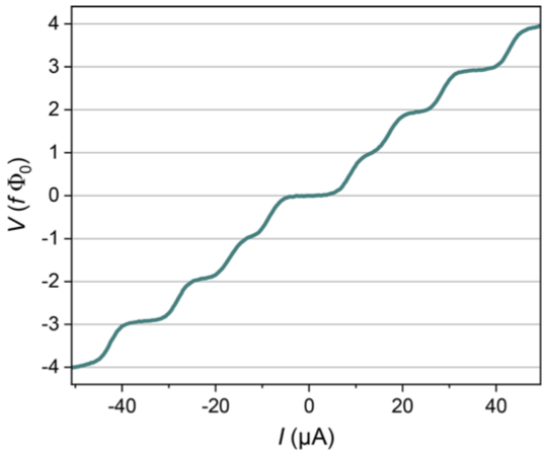

Figure 2.7: *Example of Shapiro Steps, taken from Blom et al. (2021) [18].*

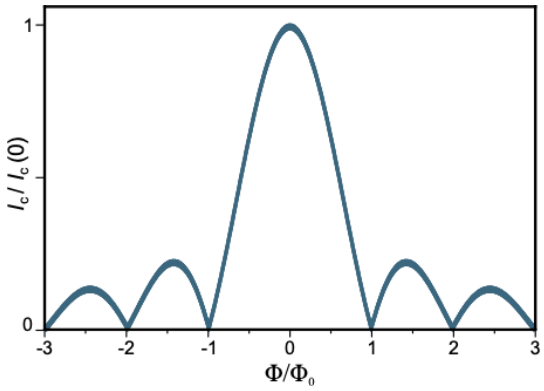

Figure 2.8: *Simulated Frauenhofer diffraction pattern in a standard Josephson junction [17].*

tion pattern on a screen standing behind the slit, showing a phase variation of scattered waves in real space. Similarly, the critical current in a Josephson junction will show a diffraction pattern in phase space, when applying a magnetic field perpendicular to it (see figure 2.8).

The diffraction pattern is caused by the self-interference of shielding currents in the junction. These currents change the phase coherence and subsequently the phase difference in equation 2.2. Yet, integer values of the magnetic flux quantum can still penetrate the junction in the form of Josephson vortices, leading to the following equation for the diffraction pattern:

$$I_c = I_c^{\max} \left| \frac{\sin(\frac{\pi\Phi}{\Phi_0})}{\frac{\pi\Phi}{\Phi_0}} \right| . \tag{2.3}$$

Diffraction patterns are an essential tool in studying Josephson junctions. Their shape, symmetry, and magnitude allow for the deduction of various properties. Specifically in the case of building superconducting memory devices, they provide a means to compare the behavior of a junction in its different states. It can establish the quality of a memory device by comparing the contrast between two patterns (such as in figure 2.4), but it can also provide evidence for the effects of stray fields from the ferromagnetic layer(s) of a junction.

Chapter 3

Design Process

For our memory device to function, we need to find a bistable ferromagnetic geometry to complement our superconductor in the SFS Josephson junction. Bistability in this context refers to two distinct magnetic textures within the same geometry that minimize the total energy of the system at remanence. Earlier work at Leiden University by Lahabi [17] and Van Dinter [19] with circular SFS Josephson junctions demonstrated the potential for a SCM device by displacing a magnetic vortex in the F-layer of the junction. Circular disks, however, do not show two stable remanent states due to their high symmetry and boundary curvature, forcing magnetic spins to locally align along the edge. To improve upon this work, we focus on finding a suitable elliptical geometry instead. Besides a well documented double-vortex ground state [20–23], the increased elongation of an ellipse compared to a circle could be the basis for a stable fully magnetized state containing no magnetic vortices.

3.1 Micromagnetic Simulations

The desired properties of our ferromagnet are heavily dependent on its physical size and shape. [20] In order to find the specific configuration that meets our requirements, we rely on micromagnetic simulations. The benefits of this choice are twofold: it saves great amounts of time to optimize the size of a device before fabrication, and the information gained from simulations at the very least enhances the interpretations from experiments and at best verifies them.

In the following subsections, we briefly introduce the fundamental physical concepts that form the foundation for micromagnetic simulations before we describe how we used them to find our elliptical disk geometry.

3.1.1 Theoretical Foundation of Micromagnetic Simulations

Micromagnetic simulations are based on three key principles. The first is that magnetic materials can be divided into microscopic rectangular* domains with a net magnetization. The size of these domains is governed by the *exchange length*, which can be interpreted as the distance

*Cells need not be cubic. In certain applications, it can save significant computation time to increase the sides of the cells along one or two dimensions.

over which exchange interactions take place. In the case of thin films, this length scale is given by

$$l_{\text{ex}} = \sqrt{\frac{2A}{\mu_0 M_s^2}}\,. \tag{3.1}$$

Here A is the exchange stiffness in J/m and M_s is the saturation magnetization in A/m. [24] Both of these quantities are material-specific: A gives a measure for the strength of the interaction between neighboring spins taking into account the crystal structure of the material, while B defines the maximum magnetization the material can sustain, which is often realized by aligning all magnetic spins. For a simulation to be physically accurate, the chosen cell size should not exceed the exchange length of the chosen material.

The second principle is that each configuration of the simulation has an associated energy value, with stable configurations corresponding to minima in this energy landscape. This energy value can be calculated with

$$E_{\text{total}} = \int \left(\varepsilon_{\text{exchange}} + \varepsilon_{\text{demagnetization}} + \varepsilon_{\text{zeeman}} + \varepsilon_{\text{anisotropy}}\right) dV\ . \tag{3.2}$$

The first term produces the energy from exchange interactions between spins within the distance defined by equation 3.1, which decreases by local spin alignment. The second term arises from the interaction with the demagnetizing field (commonly referred to as stray field). This energy decreases as spins align parallel with the surface of the geometry. The third term accounts for interaction between the spins and an externally applied field, which also decreases as spins align with it. Finally, the anisotropy term accounts for cases where the crystal structure in a material creates a magnetic easy axis, making magnetization in one direction more energetically favorable than others. In simulations, these effects are combined into an effective field $\boldsymbol{B}_{\text{eff}}$.

The final principle is that the simulation evolves with a cell-specific time evolution algorithm. The Landau-Lifshitz-Gilbert (LLG) equation suites this purpose perfectly. Despite being designed in 1955, the equation still forms the basis of most micromagnetic simulations today. The LLG equation is defined as:

$$\frac{\partial \mathbf{m}}{\partial t} = -\gamma \left(\boldsymbol{m} \times \boldsymbol{B}_{\text{eff}} - \alpha \boldsymbol{m} \times \frac{d\boldsymbol{m}}{dt} \right) \tag{3.3}$$

with $\boldsymbol{m}(\boldsymbol{r}, t)$ the local magnetization, γ the gyromagnetic ratio, $\boldsymbol{B}_{\text{eff}}$ the effective field as defined by the contributions in equation 3.2, and α a dimensionless damping parameter. This equation of motion combines the precession of a magnetic spin around an effective field by Larmor precession (first term) with a dampening term. Naturally, systems tend to relax to a state where the magnetic spins are aligned with the effective field.

3.1.2 Implementation with MuMax^3

For our design process, we used the GPU-accelerated program MuMax^3 as its highly parallelized design makes it possible to simulate geometries relatively quickly on non-specialized hardware. [25]

Instead of the LLG equation, MuMax^3 uses the explicit form of the Landau-Lifshitz (LL) torque as the basis for its simulations:

$$\frac{\partial \mathbf{m}}{\partial t} = \boldsymbol{\tau} = \gamma \frac{1}{1+\alpha^2}(\boldsymbol{m} \times \boldsymbol{B}_{\text{eff}} + \alpha(\boldsymbol{m} \times (\boldsymbol{m} \times \boldsymbol{B}_{\text{eff}}))) \,. \tag{3.4}$$

This version of the LL-equation does not depend explicitly on time, decreasing the complexity of finite-element calculations. MuMax^3 advances the LL-equation with Runge-Kutta methods and stable points are found by advancing the equation until both the energy and the torque have decreased into a numerical noise floor.

A number of physical quantities can be extracted from MuMax^3. At each simulation step, the program can output global parameters like net magnetization, energies, and max torque. Perhaps even more useful is the possibility to output spatially distributed parameters such as spin magnetization as a `[x,y,z,3]` tensor, where `[x,y,z]` are the physical bounds of the simulation.

This feature extends to cells that do not reside in the magnetic geometry; one can define multiple regions in simulation space with different magnetic properties. Consequently, we define a region with the to-be simulated ferromagnetic geometry and a second region surrounding it representing vacuum. MuMax^3 then automatically calculates the spatial distribution and strength of stray fields originating from the spin texture in the ferromagnet. In the context of SFS Josephson junctions, which are highly sensitive to magnetic fields (see section 2.3), this is an extremely useful feature. We can calculate how the magnetic field in the junction area changes due to the spin texture of the ferromagnetic layer. Mathematically, this can be expressed by a sum over all field elements inside the junction area.

$$\Delta B = \frac{\Phi}{A_J} = \frac{1}{A_J} \sum_{i \in A_j} b_{z,i} \cdot a_i \,. \tag{3.5}$$

Here A_J is the junction area, a_i is the area of cell i, and Φ is the total magnetic flux penetrating it. The sum is over the local demagnetization field strengths perpendicular to the trench for all cells confined to the area A_J. Because all cells have identical size, we can simplify this to

$$\Delta B = \frac{a}{A_J} \sum_{i \in A_j} b_{z,i} = \frac{1}{N} \sum_{i \in A_j} b_{z,i} \,, \tag{3.6}$$

with N the number of cells in the junction area. In essence, equation 3.6 is the geometric average of the demagnetization field perpendicular to the junction.

To find a bistable magnetic geometry, we focus on a specific type of simulation: initialize a particular elliptical geometry, study whether it exhibits two stable and sufficiently distinct magnetic states, and verify that they can be switched between by applying an external magnetic field. Stability in this context does not merely mean that the state energies are significantly different, but additionally that the states are not easily perturbed by a small external field. The starting point of the search is at ellipses with a fixed thickness of 13 l_{ex} and a major axis length $\geq 160\, l_{\text{ex}}$, inspired by earlier simulation work by Novais et al. [20]

To initialize the simulations specifically for our material of choice - cobalt - we set the material-specific parameters to $A = 3 \times 10^{-11}$ J/m and $M_s = 1.4 \times 10^6$ A/m [26], with cubic cells with sides of 5 nm. Although MuMax^3 is capable of incorporating magnetic anistropies, we

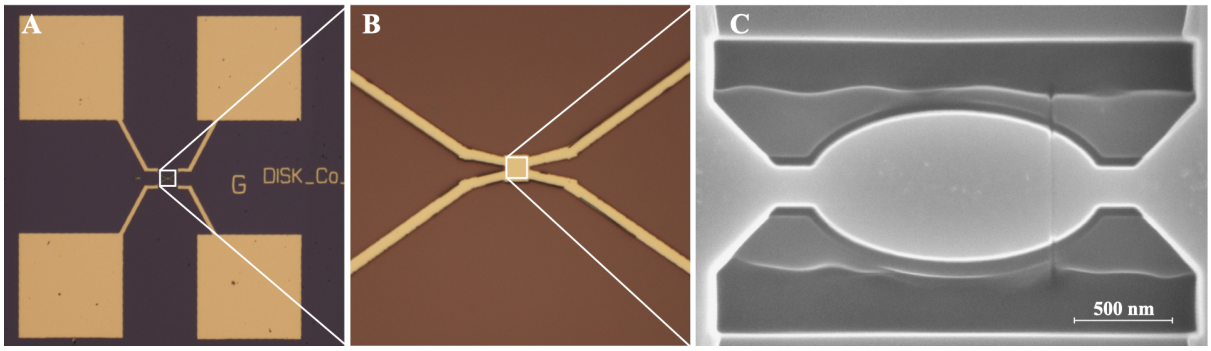

Figure 3.1: *(A-B) Optical microscope image of the full device design with four contact pads connected to a small centered structure. (C) Scanning electron microscope image of the final structure after focused ion beam milling.*

set the anisotropic parameters to zero. As will be discussed in section 3.2, we fabricate our devices by sputtering, which inherently yields a polycrystalline structure. The anisotropies of each randomly oriented crystal is averaged out on the scale of the device. Finally, we set the damping constant in equation 3.4 to $\alpha = 0.5$ in order to let the system relax into equilibrium faster. For dynamic simulations α should be set at a lower value.

3.2 Fabrication

The bilayer SFS Josephson junction consists of thin films of cobalt-niobium with the latter acting as the two superconducting electrodes and the former as the ferromagnetic weak link.

The material choice was determined in large part by practical considerations. Niobium has a relatively high superconducting critical temperature at atmospheric pressure [27] and the cobalt is a strong ferromagnet with a high Curie temperature of 1400K, which is more than enough for room-temperature memory storage applications.

Fabrication involves spin coating a silicon wafer with negative resist and carving out a rough pattern with electron beam lithography. The cobalt and niobium thin films are sputtered in a UHV chamber with argon gas at 4.0 ± 0.1 μbar. To protect the films from crystal oxidation, a 10 nm gold capping layer is sputtered on top. The microscale memory element is formed at the 5x5 μm center pad by focused ion beam (FIB) milling using gallium ions. Likewise, the off-center trench completing the Junction is created by FIB milling the upper niobium layer. Figure 3.1 A and B shows the large and rough structure containing contact pads and electrical leads to the device. Figure 3.1C shows the elliptical memory element.

Chapter 4

Results

In this chapter, we present the results of our design and test process. Because these two processes have mostly been run in parallel, we present most of our experimental results in tandem with the simulations that preceded their investigation.

4.1 Final Design

We designed the physical dimensions of our device based on results from micromagnetic simulations. We found that thin elliptical Cobalt disks with an axis ratio of 2 and a thickness of 65 nm exhibit two distinct stable magnetic states for major axis lengths between 1500 nm and 2000 nm, visible in figure 4.1 A and B. In one state, the magnetic spins are aligned along the major axis, while in the other two clear vortices are present. We call these the Zero Vortex (0V) and Two Vortex (2V) state, respectively. The stability of these two states is greatly increased by the presence of contacts (see appendix B for more information).

We designed a Niobium-Cobalt bilayer device with major axis length of 1500 nm and layer thicknesses of 50 nm and 65 nm, respectively. We added a 15 nm-wide trench cutting through the Niobium layer to produce a SFS Josephson junction. Rather than putting the trench in the center, we put the trench approximately 220 nm from the side of the device to align it with one of the magnetic vortices, as seen in figure 4.1.

We verify the superconducting nature of the device by measuring its resistance during the transition into superconductivity, repeating the measurement in the second state, shown in figure 4.2A. We see that the device becomes fully superconducting through two transitions in the 2V-state below 2 K, while in the 0V-state the resistance stays at a constant 200 mΩ. This measurement already shows a clear contrast in critical current, allowing for a electrical determination of the magnetic state.

Although a double transition is a distinctive feature in Josephson junctions, we enhance our verification by measuring an I-V while irradiating our device with a 1.5 GHz antenna at 1.6 K. We would expect to find Shapiro Steps at exact intervals of $f\phi_0$, with f the radiation frequency and ϕ_0 being the flux quantum $h/2e$. Figure 4.2B shows that we indeed found these characteristic Shapiro Steps, confirming without a doubt that our device contains a Josephson junction.

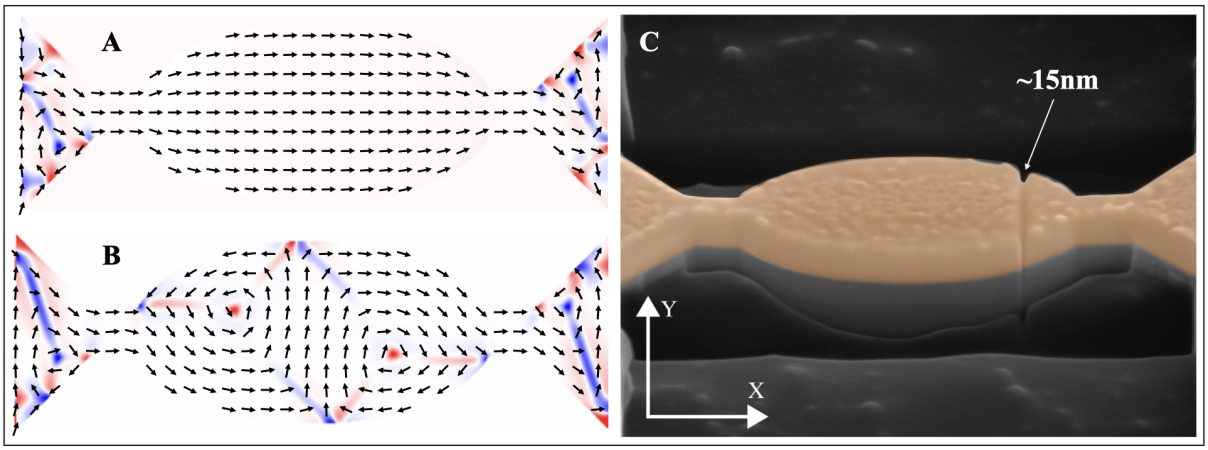

Figure 4.1: *Design process of the device. Figures A and B show the two simulated magnetic states, denoted Zero Vortex (0V) State (A) and Two Vortex (2V) State (B). The local magnetization in the x,y-plane is represented by the arrows, while the z-component is represented by the colors. (C) Guided by these results we fabricated a device with dimensions of 1500 nm by 750 nm, with a 15 nm trench located near the position of a vortex core. See appendix A for an overview of all fabricated devices.*

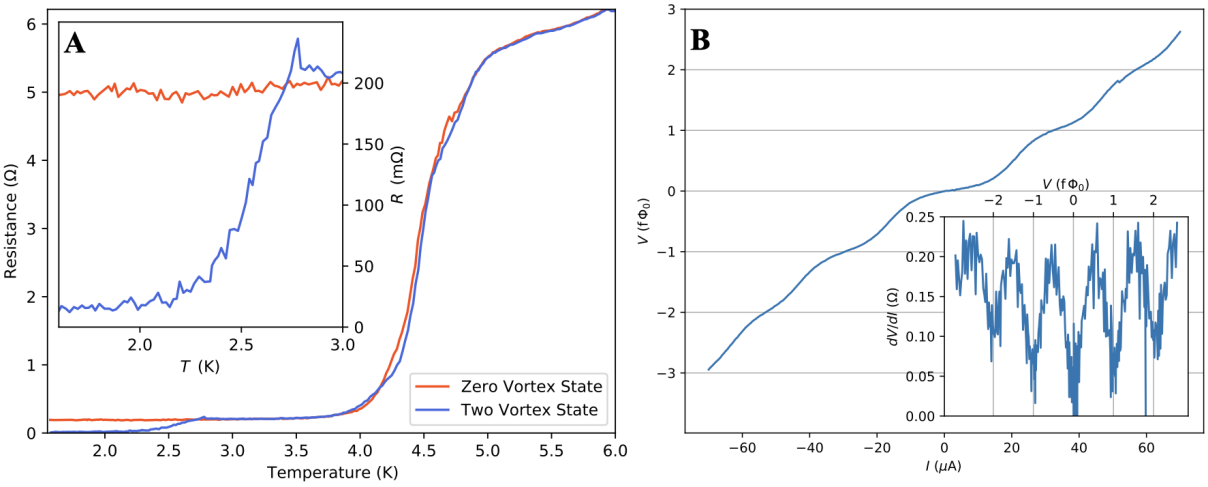

Figure 4.2: *(A) Resistance versus temperature of the elliptical device. The inset shows a major difference in behavior of the device between the two magnetic states. (B) Detection of Shapiro Steps at 1.6K while irradiated at 1.5 GHz at -7 dBm or 0.2 mW. The inset shows resistance as a function of measured voltage.*

4.2 Two-State Switching

The switching procedure between the two magnetic states involves applying an external magnetic field. Ideally, the required field strength is large enough that the device can withstand small disturbances, but not so large that one requires impractically large fields. Using micromagnetic simulations we designed our device to require switching fields within the sweet-spot range by investigating how the device responds to increasing external fields either along the x or y axis (parallel and perpendicular to the long elliptical axis, respectively), see figure 4.3 B and D.

The external field slowly perturbs the magnetic spin texture until it finally buckles into the adverse state. The simulation predicts that switching from the 0V to 2V-state occurs at an external field strength of approximately 55 mT along the y-axis. Similarly, a field of approximately 25 mT along the x-axis should be sufficient for returning to the 0V-state. For reference: the magnet

array in an Apple iPhone 12 produces a magnetic field of 5 mT. [28]

We verify these findings by performing these so-called in-plane sweeps experimentally. While keeping our device at a constant temperature of 1.6 K, we apply increasing fields along the x and y-axes of the device with steps of 5 mT. After every field step, we deduce the critical current of the junction by measuring an I-V and calculating the differential resistance. We define the critical current as the positive current range at which the electrical resistance is less than 250 mΩ. The results are shown in figure 4.3 A and C.

We clearly see that in both sweep directions, once a specific field strength is reached, the critical current changes dramatically and is retained once the field is removed. Crucially, at zero field the critical current changes by a factor of five, making the states highly distinguishable. Finally, we see that the required field strength of this dramatic shift is in accordance with our simulations within a factor of 1.5. Based on these observations, we conclude that the properties of the device have changed primarily as a result of a switch in magnetic texture in the ferromagnetic layer of the junction.

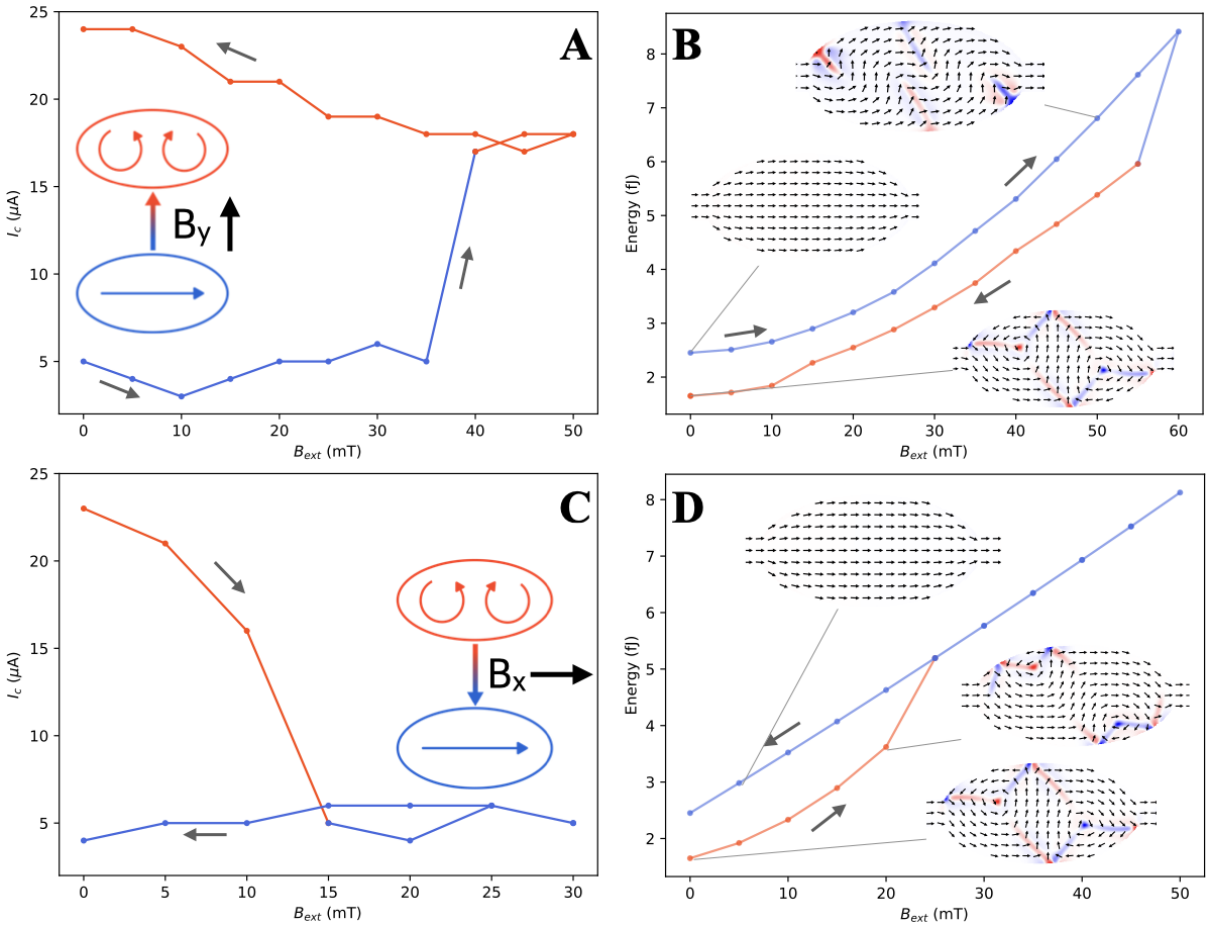

Figure 4.3: *In-plane sweeps as performed in measurements (A and C) as well as in micromagnetic simulations (B and D). The experimental results show measured critical current as a function of applied field, while the simulation results show total state energy (defined by equation 3.2) as a function of applied field. The top row shows a field sweep along the y-axis that causes the transition from the 0V to 2V-state. The bottom row shows the same sweep but along the x-axis.*

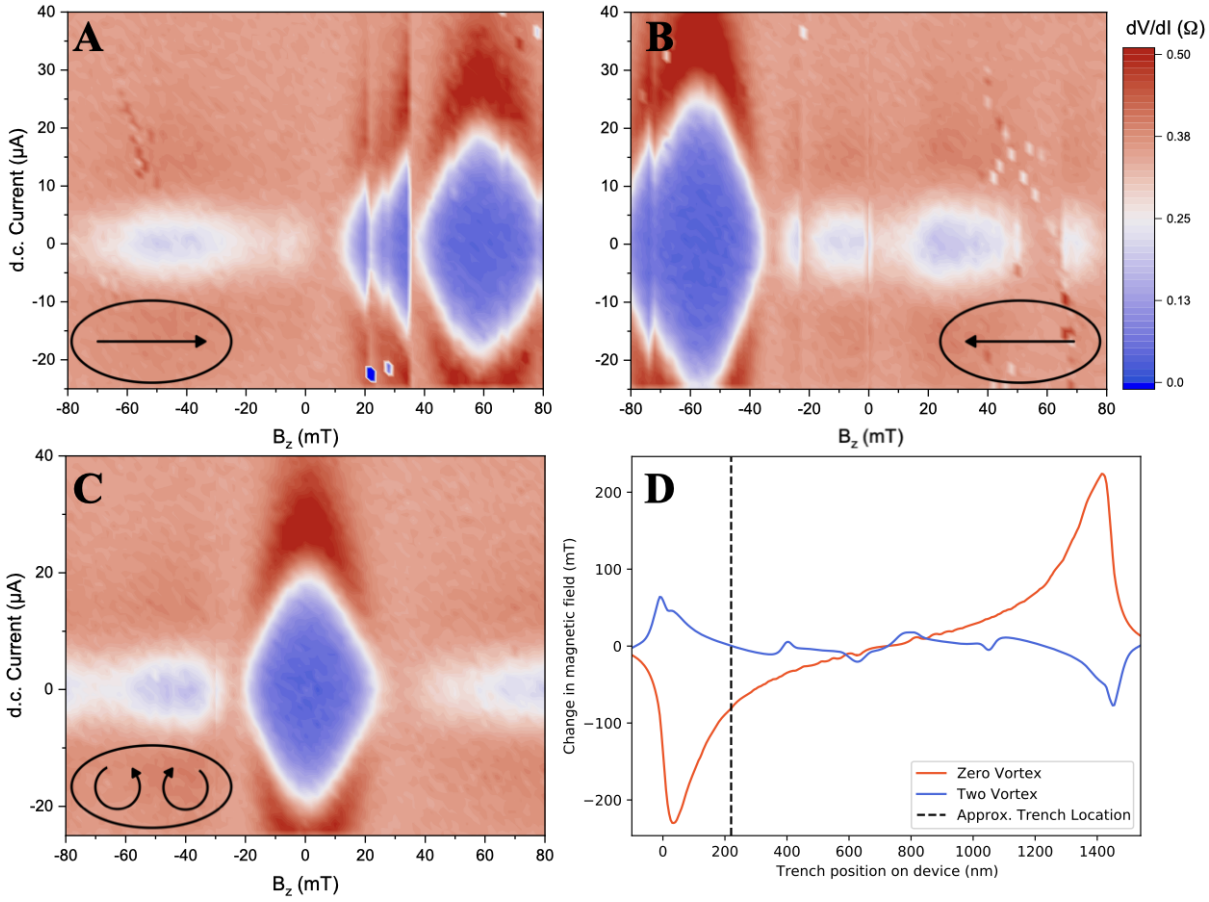

Figure 4.4: *(A-C) Out-of-plane interference patterns. We set an external field and measure the resistance as a function of d.c. current in our device. The glitches in the pattern are due to superconducting vortices. A and B show the measured pattern in the zero-vortex state and C shows the pattern in the two-vortex state. (D) Calculated expected pattern shift due to stray fields. Appendix C offers supplementary diffraction patterns from other sample devices.*

4.3 Physical Process

What process drives this massive shift in critical current? As described in section 2.3, Josephson junctions are sensitive to magnetic flux penetrating the junction area. This sensitivity is source-independent, meaning that a junction cannot distinguish between stray fields originating from its own ferromagnetic layer and externally applied fields by an experimenter. Recent work by Krasnov [29] demonstrates how stray fields distort and displace the diffraction patterns of Josephson junctions. As stated in section 3.1.2, we can actually calculate the shift in magnetic field using micromagnetic simulations. Assuming a trench width of 15 nm, we can even calculate this shift as a function of trench position on the device (see figure 4.4D).

According to the simulation result, the location of the trench on our device gives a large contrast in stray field strength between the two magnetic states, yielding a pattern shift of roughly 80 mT. In experimental out-of-plane diffraction measurements, a similar picture emerges (see figure 4.4 A-C). The peak of the diffraction pattern is centered around zero in the 2V-state, while it is shifted symmetrically by $\pm$ 60 mT in the 0V-state. Again, the experimental and simulation results are in accordance within a factor of 1.5.

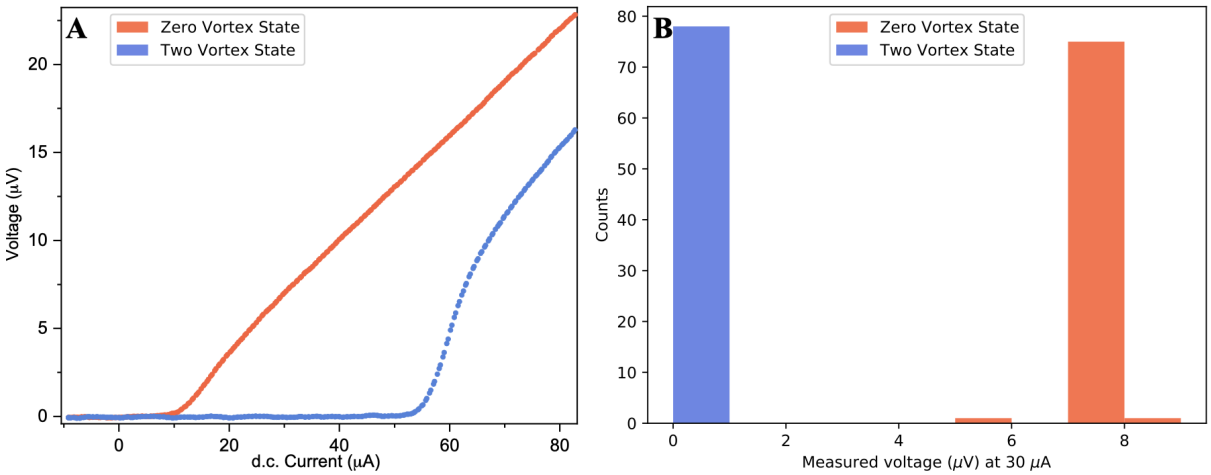

Figure 4.5: *(A) Typical I-V of our device recorded in the two states. Using these IV-characteristics we can define a read out current at which we measure a finite voltage in the 0V state, but no voltage in the 2V-state. (B) Histogram of measured voltages after repeated switching. The data points are categorized based on which state we expect the device to be in.*

4.4 Reproducibility and Volatility

For memory applications, it is insufficient to merely distinguish between two distinct states. Vitally, the memory element should be able to switch between the two states practically indefinitely. To test this reproducibility of our device in a controlled manner, we specify a *readout-current* defined by the characteristics of the two states. Specifically, we take an I-V for both states and choose a current at which the difference in voltage between the states is sufficiently large, see figure 4.5A. For this device we choose a readout-current of 30 μA.

We probe the reproducibilty of the memory element as follows: prepare the device in one state with a writing field of 40 mT* in the relevant direction (as described in section 4.2) and subsequently measure the voltage at a current of 30 μA. This procedure is repeated 156 times. The test is whether the voltage changes after applying a switching field and whether it changes in a predictable fashion.

Figure 4.5B shows that the measurement is remarkably reproducible: we see two clearly distinct measurement peaks which match their corresponding expected state. In the context of memory applications, this complete absence of overlap between read-out voltages is vital.

We enhanced this result with two additional experiments. One experiment involves heating the device to 8 K (far above its superconducting transition) and afterwards cooling it down to 1.6 K in-between switching fields. If the device is temperature-volatile, we would expect to get different results before and after the temperature shift. The other experiment tests the stability by applying fields of 10 mT in-between the switching fields of 40 mT. Here we test whether the states remain unperturbed while subjected to smaller fields than the switching fields. Both of these experiments give satisfactory result: we detect no sign of temperature-based volatility or any evidence to suggest that the device switches or otherwise changes state when subjected to fields below 10 mT.

*This field strength is chosen based on the observation (seen in figure 4.3 A and C) that switching in both directions should occur below 40 mT.

Chapter 5

Conclusion and Outlook

At the start of chapter 2, we mention four criteria for an implementable superconducting memory device: separability, switchability, non-volatility, and scalability. While other designs fulfill some of these criteria, none have so far managed to succeed on all counts. In this thesis, we have proposed a novel design for a SCM device. Instead of storing information in multiple ferromagnetic layers of a Josephson junction, we store information in a single elliptical ferromagnetic layer using spin texture.

The junction is designed using micromagnetic simulations to find geometries with two stable magnetic states with associated switching fields. We introduce a technique to quantify the expected shift in diffraction pattern due to stray fields from the ferromagnetic layer in a junction. This novel technique can be used as part of the design process in future projects involving SFS Josephson junctions.

We confirm through both experimental and simulation results that our elliptical SFS junction shows two distinct ferromagnetic states, named the zero vortex (0V) and two vortex (2V) states, with a large contrast in stray field strength between them. The stray fields suppress the critical current in the 0V-state compared to the 2V-state, leading to a change in critical current of a factor 5 at zero field. Furthermore, we show that switching between the two states is possible in a reliable and repeatable fashion by applying fields of 40 mT. We therefore conclude that our devices passes the first three criteria of an implementable memory device.

The challenge that remains is scaling up this device to the scale required for future data centers. Evidently, this requires a different switching mechanism than the one used here. Applying a switching field to a large array of our memory devices would globally switch all bits between a logical ”0” and ”1” state. However, alternative switching mechanisms could be implemented: both radio frequency radiation induced switching of magnetic texture as locally induced fields by nanowires are possible pathways to scaling up our memory design. Combining these techniques could further the development progress for superconducting computing, helping us reach the energy savings required for a sustainable future.

Chapter 6

Acknowledgments

Doing a research project during a pandemic has been a weird experience. As a physics student, you expect to spend most of your time in research on headache-inducing but fascinating physics, with the eventual disappointment of the mundane nature of some of your days. But 2020 and 2021 had other plans. Instead of excitement over research results, I experienced fatigue from seemingly never-ending waves of infections. Where coming to the lab once bore fruitful discussions, this year it felt like entering a ghost town. Working from home decreased productivity, adding to the usual pressure of a research project.

This has not been an easy year, to say the least, but it could have been worse. None of my friends or family has fallen seriously ill, and no relationships have been broken over different views on the gravity of the pandemic or the efficacy of vaccines, something that apparently cannot be taken for granted. The pandemic provided a test of character for a lot of people, and I am grateful that my colleagues and supervisors passed with flying colors.

I would like to thank Dyon van Dinter, a long time friend and first time colleague, for showing me the reigns in the first weeks of my internship. The start he gave me has proven invaluable during the project. I would like to thank Remko Fermin for always finding time to help me with my many questions and for urging me to take a vacation when my productivity had taken a turn. But most importantly, I will miss Remko's masterful baking skills. His tasty delights always managed to summon life to the empty halls of the Huygens Laboratory. Kaveh Lahabi's passion for superconductivity hasn't gone unnoticed. I am grateful for being exposed to outbursts of this passion on numerous occasions. When not talking about physics, I found in Kaveh a companion for a shared hobby: digital photography and cinematography. Mostly I am grateful for Kaveh and Remko's empathetic spirit, alleviating the pressure I am known to put on myself.

I would further like to thank Douwe Scholma for his indisputable support in learning to use the lab equipment, and Wolfgang Löffler for taking the time to be the second corrector for my thesis. Finally I would like to thank my supervisor Jan Aarts; although the pandemic and Jan's duties as director made it impossible to get to know each other as well as I would have wished, the few interactions we had have been valuable and inspiring.

Appendix A

Overview of Used Samples

During this research project, we fabricated a large number of samples, with various degrees of success. We have attempted to condense the amount of samples used in this thesis to a minimum, based on the amount of data available for each sample. We ensured that both presented in-plane and out-of-plane measurements originate from the same device. Likewise, we chose a device only for the RT and Shapiro step figure, as it was the only device where we performed Shapiro step measurements. Table A.1 shows a complete overview of all devices used. The shape (elliptical with an axis ratio of 2) is the same for all devices.

Table A.1: *Overview of devices used in this thesis.*

Identifier	Figures	Long axis (nm)	S-layer thickness (nm)	Trench depth (FIB setting)
K7A	3.1C,4.3, 4.4	1500	40	50 nm z-size
K9C	4.2	2000	50	80 nm z-size
K9F	4.1	1500	50	70 nm z-size
K9G	4.5, C.1 left	1500	50	65 nm z-size
K9H	C.1 right	1500	50	75 nm z-size

Appendix B

Stability of Magnetic States

In this appendix, we share supplementary results and lessons learned from performing micromagnetic simulations on thin elliptical cobalt ferromagnets. As mentioned in chapter 3.1.1, stable configurations of the magnetic spins correspond to minima in the energy landscape defined by equation 3.2. Specifically, the demagnetization energy density is minimized when spins are aligned along the boundary of the geometry. Clearly, the shape of a ferromagnet then greatly affects the influence of this term in the energy minimization process. For example, the curvature of a micrometer-sized circular ferromagnet produces a single stable ground state, namely a vortex state with the core centered in the circle (see figure B.1). Even after fully magnetizing the disk using a large externally applied in-plane field, the magnetic texture will relax to its vortex ground state.

This led to the motivation as stated in the introduction of chapter 3. Because an ellipse is essentially a circle that has been stretched in one direction, we hypothesized that this break of circular symmetry would have the effect of creating a second stable magnetic state in which the ellipse is fully magnetized along its longest axis. Specifically, the elongated axis could mitigate the effect of curvature in preventing a magnetized state from forming.

To simulate whether these two states exist, we initially simulated how an ellipse with a long axis of 800 nm and an axis ratio of 2 relaxes after being fully magnetized along its shortest or longest axis. We found that it relaxes into a double vortex and fully magnetized state, respectively (see figure B.2).

This positive result came with a serious caveat: we found that applying a field as small as a few millitesla to the magnetized state would immediately return it to the double vortex state. If this was indeed the case, any memory device built with this structure would be extremely sensitive to external disturbances.

To overcome this problem, we added bar-like contacts to either side of the ellipse (see for example figure 4.1), which dramatically stabilized the magnetized state. These come with the additional benefit that they are required for the transport measurements. We expect that the stability enhancement is caused by the removal of the large curvature gradient on the edges of the ellipse.

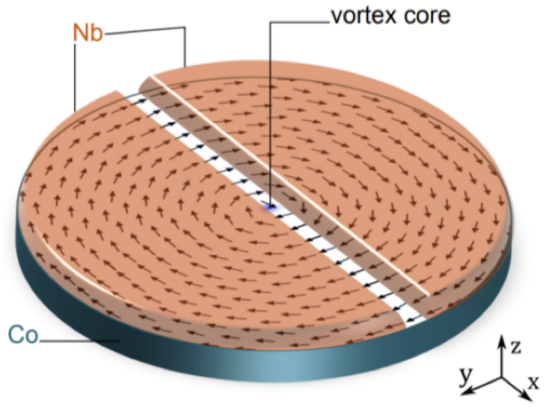

Figure B.1: *Circular SFS Josephon Junction with niobium contact and a cobalt ferromagnetic layer. The in-plane magnetic vortex spin texture is shown with arrows. Image taken from Lahabi (2018). [17]*

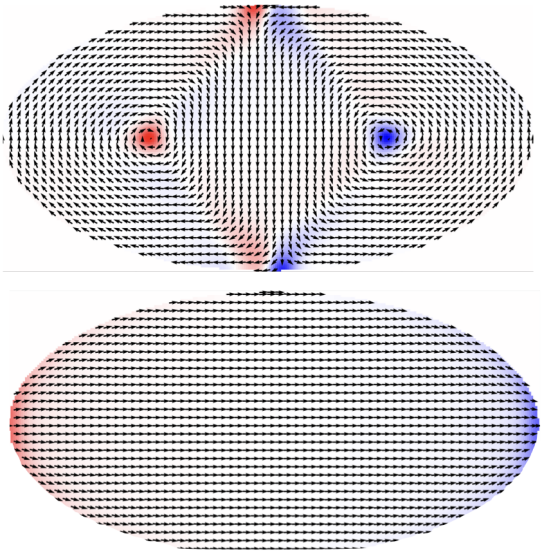

Figure B.2: *Magnetic states found by fully magnetizing an ellipse along its shortest (top) or longest (bottom) axis and letting it relax. This yields a double vortex or magnetized state, respectively.*

Appendix C

Complementary Diffraction Patterns

To show that the displacement effect due to stray fields is not unique to that specific sample shown in chapter 4, we present here the diffraction patterns of two other devices that we fabricated. The devices are identical in shape and trench location (within fabrication errors) to the one used in the main text that produced the diffraction patterns in figures 4.3 and 4.4. The difference between the samples is the depth of the trench, or, more accurately, the amount of FIB milling that was performed to form the trench. Both devices shown here have a deeper trench compared to the device used in the main text, but that sample also had a thinner niobium layer. In conclusion, accounting for fabrication differences, we find the results obtained on these sample to agree with the ones presented in the main text. See appendix C for a full overview of the used samples.

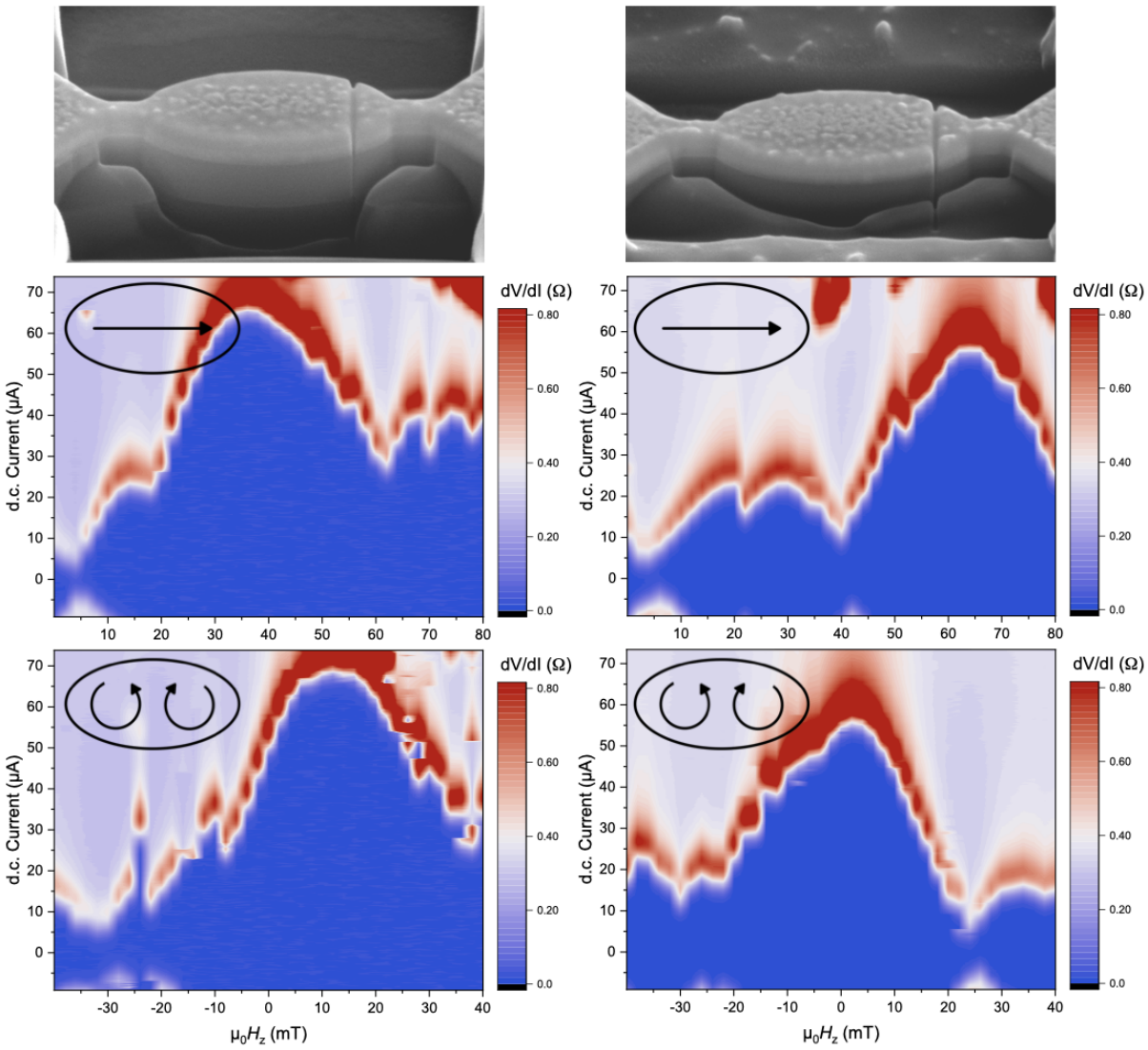

Figure C.1: *From top to bottom: SEM image of device, diffraction pattern in the magnetized state, diffraction pattern in the double vortex state. The device on the right has a deeper trench compared to the device on the right.*

Bibliography

[1] T. M. Lenton, J. Rockström, O. Gaffney, S. Rahmstorf, K. Richardson, W. Steffen, and H. J. Schellnhuber, *Climate Tipping Points - Too Risky to Bet Against*, Nature **575**, 592 (2019).

[2] S. Lange, J. Pohl, and T. Santarius, *Digitalization and Energy Consumption. Does ICT Reduce Energy Demand?*, Ecological Economics **176**, 106760 (2020).

[3] N. Jones, *How to Stop Data Centres from Gobbling up the World's Electricity*, Nature **561**, 163 (2018).

[4] A. Andrae and T. Edler, *On Global Electricity Usage of Communication Technology: Trends to 2030*, Challenges **6**, 117 (2015).

[5] *Electricity Market Report - July 2021*, Technical report, IEA, Paris, 2021.

[6] C. L. Ayala, T. Tanaka, R. Saito, M. Nozoe, N. Takeuchi, and N. Yoshikawa, *MANA: A Monolithic Adiabatic iNtegration Architecture Microprocessor Using 1.4-zJ/op Unshunted Superconductor Josephson Junction Devices*, IEEE Journal of Solid-State Circuits **56**, 1152 (2021).

[7] B. A. Butters, R. Baghdadi, M. Onen, E. A. Toomey, O. Medeiros, and K. K. Berggren, *A Scalable Superconducting Nanowire Memory Cell and Preliminary Array Test*, Superconductor Science and Technology **34**, 035003 (2021).

[8] T. Golod, A. Iovan, and V. M. Krasnov, *Single Abrikosov Vortices as Quantized Information Bits*, Nature Communications **6**, 8628 (2015).

[9] N. Satchell, P. M. Shepley, M. Algarni, M. Vaughan, E. Darwin, M. Ali, M. C. Rosamond, L. Chen, E. H. Linfield, B. J. Hickey, and G. Burnell, *Spin-Valve Josephson Junctions with Perpendicular Magnetic Anisotropy for Cryogenic Memory*, Applied Physics Letters **116**, 022601 (2020).

[10] L. Parlato, R. Caruso, A. Vettoliere, R. Satariano, H. G. Ahmad, A. Miano, D. Montemurro, D. Salvoni, G. Ausanio, F. Tafuri, G. P. Pepe, D. Massarotti, and C. Granata, *Characterization of Scalable Josephson Memory Element Containing a Strong Ferromagnet*, Journal of Applied Physics **127**, 193901 (2020).

[11] I. P. Nevirkovets and O. A. Mukhanov, *Memory Cell for High-Density Arrays Based on a Multiterminal Superconducting-Ferromagnetic Device*, Physical Review Applied **10**, 034013 (2018).

[12] R. d. A. Prada, T. Golod, O. M. Kapran, E. A. Borodianskyi, C. Bernhard, and V. M. Krasnov, *$YBa_2Cu_3O_7/La_{2/3}X_{1/3}MnO_3$ (X: Ca, Sr) based Superconductor/Ferromagnet/Superconductor Junctions with Memory Functionality*, Physical Review B **99**, 214510 (2019).

[13] A. E. Madden, J. C. Willard, R. Loloee, and N. O. Birge, *Phase Controllable Josephson Junctions for Cryogenic Memory*, Superconductor Science and Technology **32**, 015001 (2019).

[14] I. M. Dayton, T. Sage, E. C. Gingrich, M. G. Loving, T. F. Ambrose, N. P. Siwak, S. Keebaugh, C. Kirby, D. L. Miller, A. Y. Herr, Q. P. Herr, and O. Naaman, *Experimental Demonstration of a Josephson Magnetic Memory Cell with a Programmable π-Junction*, IEEE Magnetics Letters **9**, 1 (2018).

[15] B. Baek, W. H. Rippard, M. R. Pufall, S. P. Benz, S. E. Russek, H. Rogalla, and P. D. Dresselhaus, *Spin-Transfer Torque Switching in Nanopillar Superconducting-Magnetic Hybrid Josephson Junctions*, Physical Review Applied **3**, 011001 (2015).

[16] M. Tinkham, *Introduction to Superconductivity, Second Edition*, Dover Publications Inc., Mineola, New York, 2004.

[17] K. Lahabi, *Spin-Triplet Supercurrents of Odd and Even Parity in Nanostructured Devices*, PhD thesis, Leiden University, 2018, ISBN: 9789085933755.

[18] T. J. Blom, T. W. Mechielsen, R. Fermin, M. B. S. Hesselberth, J. Aarts, and K. Lahabi, *Direct-Write Printing of Josephson Junctions in a Scanning Electron Microscope*, ACS Nano **15**, 322 (2021).

[19] D. van Dinter, *Static and Dynamic S/F/S Junctions*, Master's thesis, Leiden University, 2021.

[20] E. R. P. Novais, P. Landeros, A. G. S. Barbosa, M. D. Martins, F. Garcia, and A. P. Guimarães, *Properties of Magnetic Nanodots with Perpendicular Anisotropy*, Journal of Applied Physics **110**, 053917 (2011).

[21] T. Zeng, Y. Zhou, K.-W. Lin, P.-T. Lai, and P. W. T. Pong, *Magnetic-Field-Sensing Mechanism Based on Dual-Vortex Motion and Magnetic Noise*, Journal of Applied Physics **115**, 17D142 (2014).

[22] B. Hong, T. Hayward, C. Barnes, and J.-R. Jeong, *Double Vortex Interaction in Micron-Sized Elliptical $Ni_{80}Fe_{20}$ Elements Studied by Real-Time Kerr Microscopy*, IEEE Transactions on Magnetics **45**, 2511 (2009).

[23] K. S. Buchanan, P. E. Roy, F. Y. Fradin, K. Y. Guslienko, M. Grimsditch, S. D. Bader, and V. Novosad, *Vortex dynamics in patterned ferromagnetic ellipses*, Journal of Applied Physics **99**, 08C707 (2006).

[24] G. S. Abo, Y.-K. Hong, J. Park, J. Lee, W. Lee, and B.-C. Choi, *Definition of Magnetic Exchange Length*, IEEE Transactions on Magnetics **49**, 4937 (2013).

[25] A. Vansteenkiste, J. Leliaert, M. Dvornik, M. Helsen, F. Garcia-Sanchez, and B. Van Waeyenberge, *The design and verification of MuMax3*, AIP Advances **4**, 107133 (2014).

[26] J. M. D. Coey, *Magnetism and Magnetic Materials*, Cambridge University Press, Cambridge, 2010.

[27] D. K. Finnemore, T. F. Stromberg, and C. A. Swenson, *Superconducting Properties of High-Purity Niobium*, Phys. Rev. **149**, 231 (1966).

[28] F. Nadeem, A. Nunez Garcia, C. Thach Tran, and M. Wu, *Magnetic Interference on Cardiac Implantable Electronic Devices From Apple iPhone MagSafe Technology*, Journal of the American Heart Association **10** (2021).

[29] V. M. Krasnov, *Josephson Junctions in a Local Inhomogeneous Magnetic Field*, Physical Review B **101**, 144507 (2020).